Two-dimensional perovskite templates for durable, efficient formamidinium perovskite solar cells

Siraj Sidhik, Isaac Metcalf, Wenbin Li, Tim Kodalle, Connor J Dolan, Mohammad Khalili, Jin Hou, Faiz Mandani, Andrew Torma, Hao Zhang, et al.

▶ **To cite this version:**

Siraj Sidhik, Isaac Metcalf, Wenbin Li, Tim Kodalle, Connor J Dolan, et al.. Two-dimensional perovskite templates for durable, efficient formamidinium perovskite solar cells. Science, 2024, 384 (6701), pp.1227-1235. 10.1126/science.abq6993 . hal-04612789

HAL Id: hal-04612789
https://hal.science/hal-04612789v1

Submitted on 14 Jun 2024

HAL is a multi-disciplinary open access archive for the deposit and dissemination of scientific research documents, whether they are published or not. The documents may come from teaching and research institutions in France or abroad, or from public or private research centers.

L'archive ouverte pluridisciplinaire **HAL**, est destinée au dépôt et à la diffusion de documents scientifiques de niveau recherche, publiés ou non, émanant des établissements d'enseignement et de recherche français ou étrangers, des laboratoires publics ou privés.

S. Sidhik et al., Science, 384 (6701), pp 1227-1235 - DOI: 10.1126/science.abq6993

Two-dimensional perovskite templates for durable, efficient formamidinium perovskite solar cells

Siraj Sidhik[1,2#], Isaac Metcalf[1#], Wenbin Li[3], Tim Kodalle[4], Connor Dolan[5], Mohammad Khalili[2], Jin Hou[1], Faiz Mandani[2], Andrew Torma[3], Hao Zhang[3], Rabindranath Garai[2], Jessica Persaud[2], Amanda Marciel[2], Itzel Alejandra Muro Puente[6], G. N. Manjunatha Reddy[6], Adam Balvanz[7], Mohamad A. Alam[8], Claudine Katan[9], Esther Tsai[10], David Ginger[11], David Fenning[5], Mercouri G. Kanatzidis[12], Carolin M. Sutter-Fella[4], Jacky Even[13]* and Aditya D. Mohite[1,2]*

[1]Material Science and Nanoengineering, Rice University, Houston, TX 77005, USA.

[2]Department of Chemical and Biomolecular Engineering, Rice University, Houston, TX 77005, USA.

[3]Applied Physics Graduate Program, Smalley-Curl Institute, Rice University, Houston, TX, 77005, USA.

[4]Molecular Foundry, Lawrence Berkeley National Laboratory, Berkeley, CA 94720, USA

[5]Department of Nanoengineering, University of California, San Diego, La Jolla, CA 92093, USA.

[6]University of Lille, CNRS, Centrale Lille Institut, Univ. Artois, UMR 8181-UCCS-Unité de Catalyse et Chimie du Solide, F-59000 Lille, France

[7]Department of Chemistry, Northwestern University, Evanston, IL 60208, USA.

[8]School of Electrical and Computer Engineering, Purdue University, West Lafayette, IN, USA.

[9]Univ Rennes, ENSCR, CNRS, ISCR-UMR 6226, Rennes F-35000, France.

[10]Center for Functional Nanomaterials, Brookhaven National Laboratory, Upton, NY, USA

[11]Department of Chemistry, University of Washington, Seattle 98195.

[12]Department of Chemistry and Department of Materials Science and Engineering, Northwestern University, Evanston, IL 60208, USA.

[13] Univ Rennes, INSA Rennes, CNRS, Institut FOTON - UMR 6082, Rennes F-35000, France.

***Correspondence to: jacky.even@insa-rennes.fr; adm4@rice.edu**

S. Sidhik et al., Science, 384 (6701), pp 1227-1235 - DOI: 10.1126/science.abq6993

Abstract

We present a design strategy for fabricating ultra-stable, phase pure films of formamidinium lead iodide ($FAPbI_3$) by lattice templating using specific two-dimensional (2D) perovskites with FA as the cage cation. When a pure $FAPbI_3$ precursor solution is brought in contact with the 2D perovskite, the black phase forms preferentially at 100 °C, much lower than the standard $FAPbI_3$ annealing temperature of 150 °C. X-ray diffraction and optical spectroscopy suggest that the resulting $FAPbI_3$ film compresses slightly to acquire the (011) interplanar distances of the 2D perovskite seed. The 2D templated bulk $FAPbI_3$ films exhibited an efficiency of 24.1% in a p-i-n architecture with 0.5 cm^2 active area, and an exceptional durability with T_{97} of 1000 hours under 85 °C and maximum power point tracking.

Perovskite light absorbers with the chemical formula $APbI_3$ (where A is a monovalent cation) have been extensively studied in photovoltaic devices. Among the commonly used A-site cations, such as formamidinium (FA), methylammonium (MA), and caesium (Cs^+), FA has shown promising performance because of its lower bandgap (E_g), improved optoelectronic properties, and higher thermal stability compared to MA *(1)*. The larger size of the FA cation yields the Pm3m cubic perovskite lattice through close packing, rather than the lower-symmetry tetragonal (I4/mcm) lattice of $MAPbI_3$ *(2,3)*. The lower E_g value of $FAPbI_3$ results from a high degree of Pb 6s - I 5p orbital overlap and reduction of octahedral tilts. The $FAPbI_3$ lattice appears to be a polymorphous network where the average high symmetry structure results from a random distribution of local lower-symmetry (distorted) structural motifs *(4)*. The complexity of the α- (black) phase of 3D bulk $FAPbI_3$ is also reflected by the distribution of the reported average lattice parameter values ranging at room temperature (RT) from *a* ranging from 6.352 to 6.365 Å *(5,6)*.

Moreover, the high symmetry of the $FAPbI_3$ lattice comes at the expense of phase stability. The Goldschmidt tolerance factor of the black α-phase of three-dimensional (3D) $FAPbI_3$ (0.987) is at the edge of the stable range for the perovskite structure (0.8 to 1.0) because the FA cation is almost too large for the A-site *(7)*. As a result, the room temperature (RT) strain-free α-phase of $FAPbI_3$ presents vanishing shear and bulk elastic moduli, and a metastability against the reconstructive phase conversion to the yellow, photoinactive non perovskite δ-phase *(5,8)*. Alloying FA with Cs, MA, or both at the A-site can reduce the effective A-site radius of the perovskite structure and lower the tolerance factor, which improves phase stability at RT but comes at the expense of a widened bandgap *(9-11)*.

Kinetically trapping the α-phase of $FAPbI_3$ is one of the key steps to achieve stable solar cell operation at RT *(12)*. Recently, there have been several reports on FA-based perovskites which with certified power conversion efficiencies (PCEs) exceeding 25% (record 26.2%) for n-i-p *(13-20),* and 24% for p-i-n device architectures *(21-24)*, often by incorporating high concentrations of methylammonium chloride (MACl) *(25)*, formamidinium formate *(16)*, methylene diammonium dichloride *(26),* isopropyl ammonium chloride *(27)*, and methylammonium formate *(28)*, to stabilize the black phase with a E_g of 1.52 eV or higher. The large E_g (compared to the lowest-reported $FAPbI_3$ value of 1.45 eV obtained on single crystals *(5,29)*) is indicative of alloying between FA and MA at the A-site of the perovskite lattices. Other cations, such as Cs^+ *(9,30)*, and Rb^+ *(20,31)*, have also been studied for their potential to improve stability.

Nonetheless, the stability of these FA-based solar cells is still limited, specifically under temperatures exceeding 60°C and AM1.5G light illumination under operation at maximum-power-point tracking (MPPT). Recently, multiple studies have used bulky amine salts with $FAPbI_3$ to stabilize the α-phase through the formation of a metastable two-dimensional (2D) perovskite phase

(19,27,32-40). These 2D perovskites have the chemical formula $A'_2A_{n-1}Pb_nI_{3n+1}$, where A' is a bulky monoammonium cation and n controls the thickness of the perovskite layers. Inspired by this success, we opted to combine in-plane lattice matched 2D perovskites with $FAPbI_3$, to create lattice-matched interfaces using our newly introduced 2D memory seeds method, instead of employing amine salts *(41-43)*.

Here, we show that bulk $FAPbI_3$ forms a highly stable black phase at a temperature well below the δ-$FAPbI_3$ to α-$FAPbI_3$ transition temperature by templating the (001) interplanar spacing of 3D $FAPbI_3$ to the (011) interplanar spacing of a judiciously selected 2D phase (the respective Pb-Pb interatomic spacing for each structure). The $FAPbI_3$ precursors, when drop-cast over a film of Ruddlesden-Popper (RP) phase 2D perovskite $A'_2FAPb_2I_7$, where the A' cation can be butylammonium (BA), or pentylammonium (PA), converted into black phase $FAPbI_3$ at temperatures as low as 100 °C, which is well below the 150 °C temperature at which additive-free control films underwent a yellow-to-black phase transition.

From our studies of film formation using correlated wide-angle x-ray scattering (WAXS), optical absorbance, and photoluminescence (PL), we hypothesized that the resulting black $FAPbI_3$ phase exhibited a lattice constant corresponding to the $d_{(011)}$ interplanar spacing of the underlying 2D perovskite. We could also translate the 2D-templated stabilization of $FAPbI_3$ to scalable solution-processed methods by adding the pre-synthesized 2D perovskites powders (0.5-1.0 mol%) into the $FAPbI_3$ precursor solutions. In a heterophase 3D-2D FA-based film, the phase-stable 2D perovskite nucleated first because had a lower enthalpy of formation and was the phase stable at RT. The 2D structure presented a perovskite surface on which the 3D perovskite can form by distorting to adopt the underlying 2D lattice periodicity, allowing for the preferential templating of the 3D perovskite on the 2D phase during subsequent film annealing. The obtained

bulk films of $FAPbI_3$ exhibit a bandgap (E_g) of 1.48 eV and demonstrate exceptional durability under aggressive ISOS-L-2 conditions of 85ºC/AM1.5G illumination and a PCE of 24.1% in a p-i-n device architecture on a 0.5 cm^2 device area. We believe that these results validate a novel design strategy for the templated growth of 3D perovskites using designer 2D perovskites, which share a nearly identical lattice constant.

Black phase stabilization of $FAPbI_3$ with 2D perovskite template

The general design principle, the selection criteria, and proof-of-concept for the 2D perovskite-based templating of $FAPbI_3$ are shown in **Fig. 1**. **Fig. 1A** shows the in-plane lattice parameter corresponding to the Pb-I-Pb distance, along directions perpendicular to the (011) plane for the 2D $BA_2FAPb_2I_7$ perovskite and the (001) plane for the 3D $FAPbI_3$ perovskite, as a function of layer thickness (n-value) for 2D perovskites formed with a variety of A' site cations. The grey horizontal bar represents the range of reported lattice parameters for bulk $FAPbI_3$ taken single-crystal structural studies *(5,6)*. The $(011)^{2D}$ interplanar spacings were calculated from crystal structures obtained with single-crystal diffraction of each 2D perovskite. Based on the lattice parameters, we hypothesized that the lattice mismatch between the 2D and 3D perovskites must be kept low to minimize the 2D-3D interfacial energy and encourage growth through templating.

We searched for FA-based 2D perovskites with an in-plane lattice parameter close to $FAPbI_3$. As a result, we identified that 2D n=2 FA-based perovskites with the bulky cations butylammonium (BA) and pentylammonium (PA), with lattice constants of 6.359 Å and 6.364 Å respectively, were almost perfectly lattice matched with that of 3D $FAPbI_3$ lattice parameters. However, our crystal structure analysis revealed that the phenylethylammonium (PEA) and octylammonium (OA) n=2 Pb-I-Pb distance was too small (6.265 Å and 6.336 Å, lattice mismatch of 1.5% and 0.5%, respectively) to match the 3D $FAPbI_3$ structure. Notably, all the n=1 2D

perovskites considered were lattice mismatched with $FAPbI_3$ and were not viable options for templating the 3D phase.

Fig. 1B illustrates the crystal structure of α-$FAPbI_3$ and $BA_2FAPb_2I_7$ (BA n=2) 2D perovskite, with a focus on the (001) and (011) planes. The typical 2D perovskite structure of $BA_2FAPb_2I_7$ is shown, displaying the in-plane (001) and (011), and out-of-plane (200) lattice planes. **Fig. 1C** to **1F,** describes a preliminary experiment on the growth of a layer of $FAPbI_3$ on a crystal of $BA_2FAPb_2I_7$. **Fig. 1C** (schematic) and **Fig. 1D** (optical images) shows the experiment at different stages in time. We first partially covered a substrate with a film of red coloured, millimeter-scale $BA_2FAPb_2I_7$ monocrystals that were fabricated with the air-liquid interface method and spread on an indium tin oxide (ITO) glass substrate. Once these crystals were dried on a hotplate at 100ºC, we wiped away half the glass slide to create a bare glass region on about half of the glass area. We then added a few drops of $FAPbI_3$ precursor solution (composed of an equimolar ratio of FAI and PbI_2) onto the blank surface and annealed the substrate at a temperature of 100°, 125°, or 150°C (experiments shown in **Fig. 1** were performed at a substrate temperature of 100°C). The solution flowed over and react with the $BA_2FAPb_2I_7$ 2D perovskite crystal film. Upon contact with the 2D crystals, the solution spontaneously (within 10 to 15 s) transformed into a shiny black film. The same transformation was obtained for annealing temperatures of 125° and 150°C. After letting the film equilibrate for 5 min, we obtained three distinct regions on the substrate (**Fig. 1D)**.

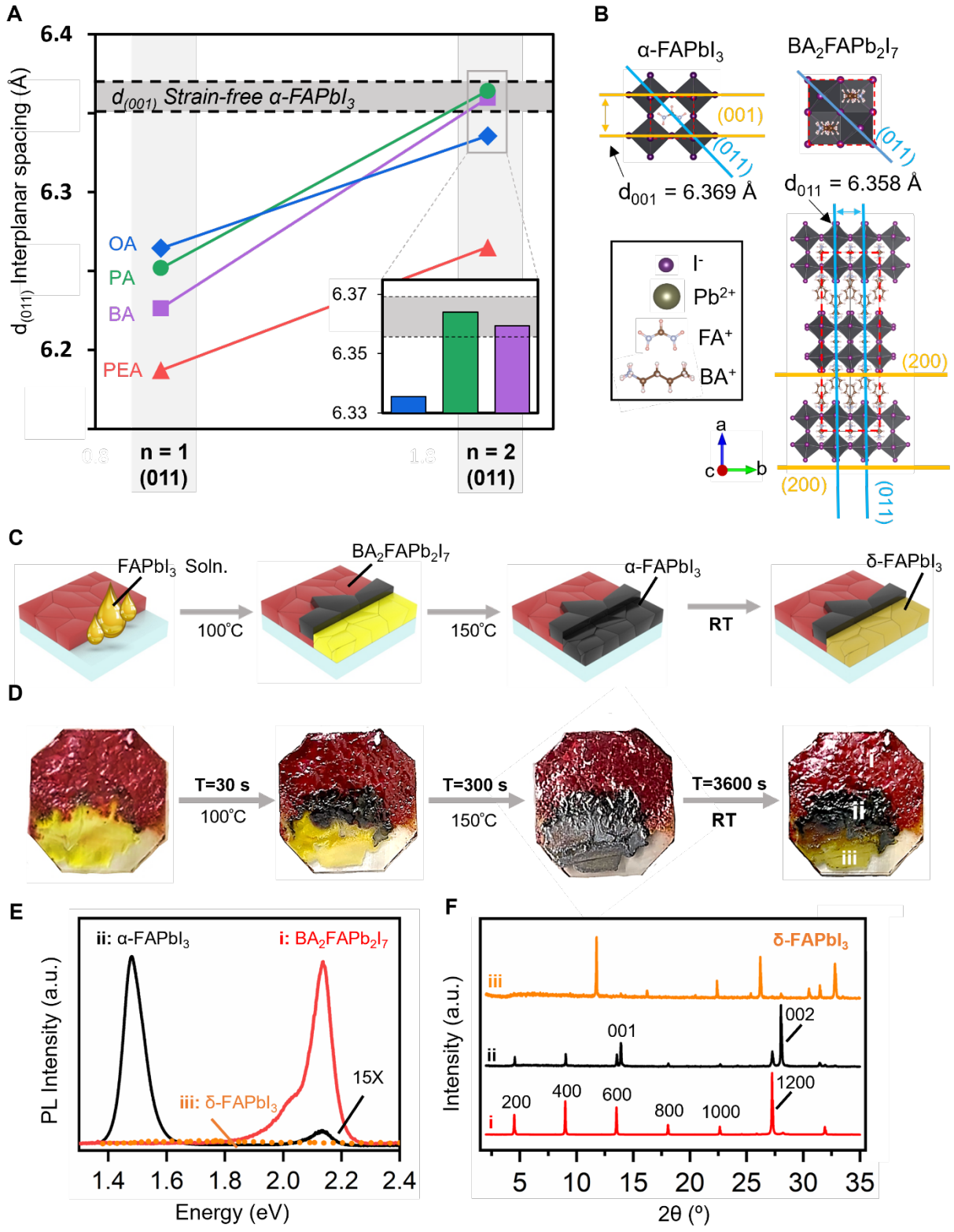

Fig. 1. Design principle and proof-of-concept for 2D perovskite lattice templating of $FAPbI_3$. **A)** The $d_{(011)}$ interplanar spacing for n=1 and FA-based n=2 2D perovskites with various A' cations: PA, BA, OA, and PEA. The range of reported values for $FAPbI_3$ $d_{(001)}$ interplanar spacing

is plotted as gray horizontal bar. Both $BA_2FAPb_2I_7$ and $PA_2FAPb_2I_7$ exhibit a $d_{(011)}$ nearly identical to the $d_{(001)}$ of $FAPbI_3$, as shown in the inset. **B)** Diagram of the unit cells of $FAPbI_3$ (left) and $BA_2FAPb_2I_7$ (right). The (001) and (011) planes are drawn for each structure. The Pb-I-Pb distance corresponds to the (001) interplanar spacing of $FAPbI_3$ and to the (011) spacing of $BA_2FAPb_2I_7$. **C**) Schematics of the templated $FAPbI_3$ drop-coating experiment. First $FAPbI_3$ precursor solution was dropped onto a glass substrate and allowed to flow over crystals of $BA_2FAPb_2I_7$. When heated, the δ-$FAPbI_3$ on top of the $BA_2FAPb_2I_7$ transformed to α-$FAPbI_3$ before the δ-$FAPbI_3$ on top of the bare substrate. Left in ambient air, the α-$FAPbI_3$ on top of the bare substrate transformed to δ-$FAPbI_3$ before the α-$FAPbI_3$ on top of the $BA_2FAPb_2I_7$. **D)** Corresponding photographs of the experiment in **(C)** showing the three distinct regions of the substrate. i: $BA_2FAPb_2I_7$ without $FAPbI_3$ solution, ii: $BA_2FAPb_2I_7$ below $FAPbI_3$ solution, and iii: $FAPbI_3$ solution on bare glass. **E)** PL, and **(F)** XRD of regions i, ii, and iii after 1 hour of exposure to ambient air, showing that the α-$FAPbI_3$ was stabilized when deposited above $BA_2FAPb_2I_7$.

The lower region of the substrate, which was originally bare, changed to a black color with partially converted α-$FAPbI_3$, at 100 °C. The middle region where the solution touched the 2D perovskite consisted of the black phase $FAPbI_3$ on the surface and $BA_2FAPb_2I_7$ below that. Finally, the top part of the substrate where the solvent did not flow remained as $BA_2FAPb_2I_7$ of millimeter-sized monocrystal film. We then left the film for 1 hour under ambient conditions. As the temperature decreased, the bottom region (originally the bare glass region) converted to the yellow phase of $FAPbI_3$ while the intermediate region remained black, suggesting the successful phase stabilization of the $FAPbI_3$. The $BA_2FAPb_2I_7$ crystal film remained unchanged over this time because of its inherent stability compared to its 3D counterpart.

We characterized the three regions of the final film using both PL and XRD measurements. **Fig. 1C** shows the PL spectra of the film obtained at the three specific regions, labelled (i), (ii), and (iii). The dominant PL of region (i) at 2.15 eV corresponded to the ground-state excitonic emission of $BA_2FAPb_2I_7$ film, accompanied by a small shoulder around 2.0 eV. The intermediate region (ii) showed strong emission at 1.48 eV corresponding to the intrinsic bandgap of the α-$FAPbI_3$ phase, with very weak emission at around 2.15 eV from $BA_2FAPb_2I_7$. These results indicated the coexistence of the bulk black phase $FAPbI_3$ 3D perovskite atop the 2D perovskite

crystal film. The presence of the 2D perovskite at the bottom was confirmed by PL measurements taken from the back of the film in region (ii), which exhibited emission solely from the 2D perovskite. As anticipated, no emission was observed from region (iii) that contained the photoinactive yellow phase of the $FAPbI_3$. Additional PL analysis for the drop-coating experiment is shown in **Fig. S1**. The detection of n=3 ($BA_2FA_2Pb_3I_{10}$) in the photoluminescence (PL) measurement acquired from the rear side provides clear evidence of the intercalation process, a phenomenon previously reported by our group (refer to **Fig. S1**) (*44*). We emphasize that the phase stabilization of $FAPbI_3$ occurred also at 100° and 125°C, which are well below the standard annealing temperatures of 150° to 160°C.

The XRD measurements presented in **Fig. 1F** validated the findings from the measurements in **Fig. 1, C to E**. Region (i) showed a pure 2D $BA_2FAPb_2I_7$ perovskite as evidenced by the strong interlayer (h00) XRD plane originating from the inorganic layer stacking. From region (ii), we found a similar XRD pattern but with the (001) and (002) diffraction planes from the α-phase $FAPbI_3$ perovskite that indicates the presence of a mixture of 2D and 3D perovskites. In region (iii), XRD showed only the presence of the δ-phase $FAPbI_3$.

The results shown in **Fig. 1** suggest that the incorporation of $BA_2FAPb_2I_7$ into $FAPbI_3$ during film formation could stabilize the perovskite phase through templating between the two structures' Pb-I-Pb interatomic distances. To test this hypothesis in $FAPbI_3$ films, 2D perovskites were added as templating agents to precursor solutions of 1:1 FAI: PbI_2 in mixed 4:1 DMF: DMSO solvent. We compared the effect of 2D perovskites with four different A'-site cations: BA, PA, OA, and PEA. Using a technique previously developed by our group *(41)*, pre-synthesized 2D crystals were added instead of the more conventional choice of A' cation halide salts. Rather than dissolving completely into constituent ions, 2D crystals in a DMF: DMSO solvent formed sub-

micrometer sized crystallites (termed as memory seeds) that preserved their perovskite structure and served as nucleation sites during film formation. These memory seeds could transfer their initial n-value to solution-processed films. However, when dissolved in a $FAPbI_3$ precursor solution rather than pure DMF: DMSO, 2D perovskite crystallites were surrounded by a high concentration of mobile A-site cations, which tended to intercalate into the seeds and increase their n-value. As a result, a 2D additive with a given A'-site cation will grow from a $FAPbI_3$ solution at its thermodynamically preferred n-value in such an environment. With this in mind, only 2D perovskites of the n-value that will precipitate from a $FAPbI_3$ solution were considered as candidates for α-phase stabilization. Through solution processing experiments summarized in **Fig. S2**, we found that each of the four RP 2D perovskites considered here grew in their n=2 phase from $FAPbI_3$ solution.

Crystallization dynamics of 2D templated $FAPbI_3$ thin films

We used our selectively designed 2D perovskites $BA_2FAPb_2I_7$ and $PA_2FAPb_2I_7$ to grow stabilized $FAPbI_3$ perovskite thin films. **Fig. 2A** visually illustrates the film formation process of $FAPbI_3$ with 2D perovskite additive, offering insight into the visible alterations that occur during the process. Perovskite films were synthesized by spin-coating with precursors of FAI: PbI_2:2D perovskite with a molar ratio of 1:1:x mol%. After antisolvent washing with diethyl ether, the thin film underwent a series of intermediate stages, which can be seen visually as changes in colour from pale red (before annealing) to dark brown, and finally to a black film when annealed at temperatures ranging from 100° to 150°C for 20 minutes.

S. Sidhik et al., Science, 384 (6701), pp 1227-1235 - DOI: 10.1126/science.abq6993

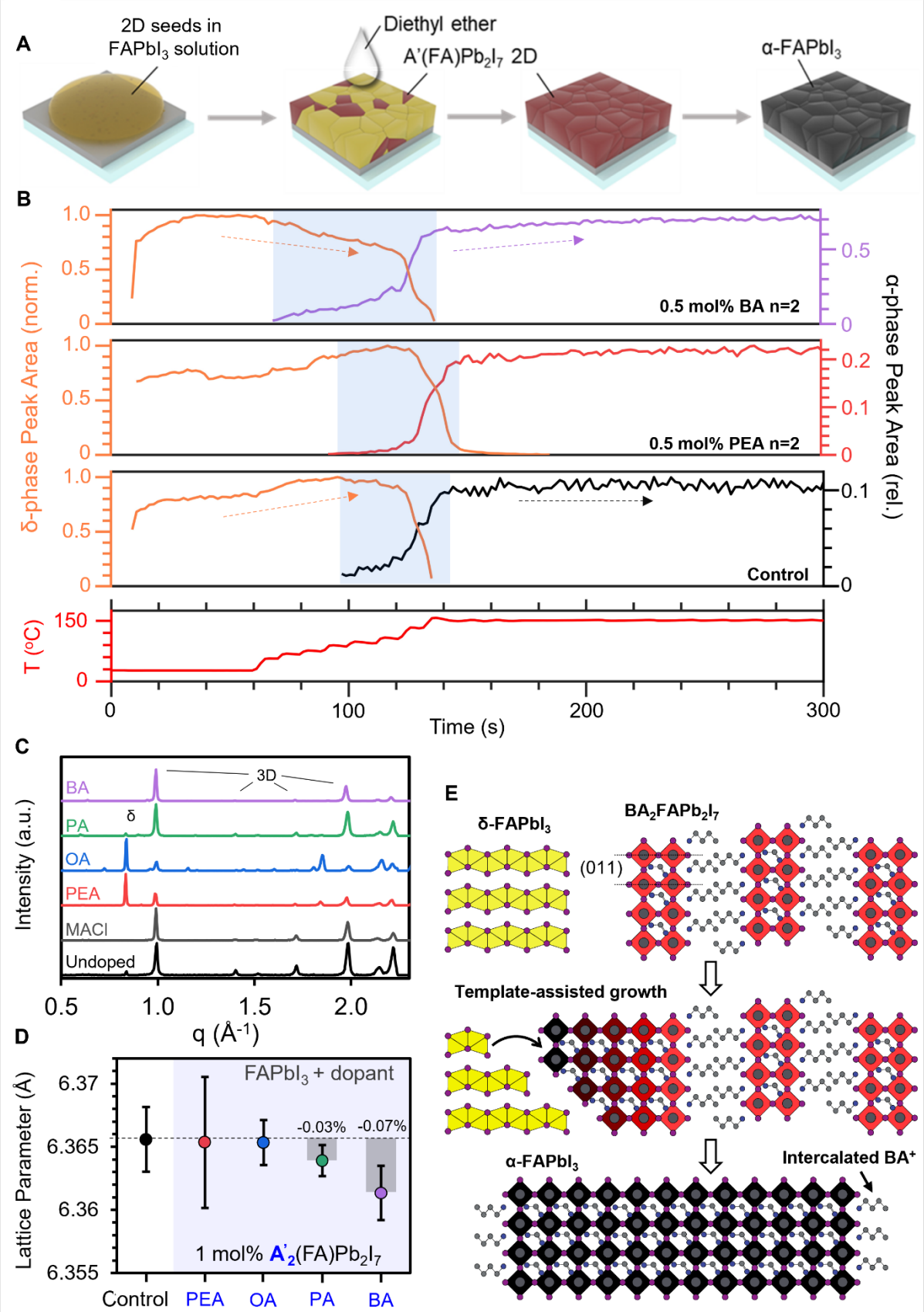

Fig. 2. 2D-stabilized $FAPbI_3$ film formation mechanism. A) Fabrication steps of a 2D crystal templated $FAPbI_3$ thin film, **B)** Integrated peak areas for the $(100)^{\delta}$ (orange, left axis) and $(001)^{3D}$ (black, right axis) peaks over time for control $FAPbI_3$ (bottom), $FAPbI_3$ with 0.5 mol% PEA n=2 added (middle), and $FAPbI_3$ with 0.5 mol% BA n=2 added (top). The $(001)^{3D}$ peak area as indicated on the right vertical axis is normalized to the maximum of the $(100)^{\delta}$ peak area. The regions between the emergence of the $(001)^{3D}$ peak and the full conversion to α-$FAPbI_3$ are highlighted in blue. **C)** Azimuthally integrated WAXS patterns averaged across the first 90 seconds of annealing after reaching 150°C for each $FAPbI_3$ additive tested (2D concentration is 1 mol%). **D)** The α-$FAPbI_3$ (001) lattice parameter for films with 1 mol% of each 2D additive, as measured on separately fabricated samples at RT. Error bars indicate standard deviation based on data from 3 to 5 samples. **E)** Schematic diagram illustrating the mechanism of lattice-matched 2D templated $FAPbI_3$ perovskite formation.

To elucidate the mechanism that produces a RT phase-stable $FAPbI_3$ film, we measured the structural dynamics of the perovskite during thin-film formation using synchrotron-based WAXS. The perovskite thin-films were deposited from solution onto a bare ITO substrate by using a robotic antisolvent pipette and a resistive-heating spin-coater in a WAXS chamber under a nitrogen atmosphere (**Fig. S3**). We first investigated the crystallization kinetics of a $FAPbI_3$ film with 1 mol% $BA_2FAPb_2I_7$ incorporated. A WAXS pattern taken during thin-film formation (**Fig. S4)** showed concentric diffraction rings corresponding to the Bragg reflections of the stacking axis diffraction planes of $BA_2FAPb_2I_7$ and α- and δ- phases of 3D-$FAPbI_3$. The diffraction peaks correspond to crystallographic planes in the 2D, α-$FAPbI_3$, and δ-$FAPbI_3$ crystal structures.

The WAXS pattern was azimuthally integrated and plotted as a function of time along with spin speed and temperature to observe the film's structural evolution (**Fig. S4**). In this in-situ experiment can be divided into four stages: (i) antisolvent dropping during spin-coating; (ii) after spin-coating but before annealing; (iii) slow annealing ramping from RT to 150°C; and (iv) constant annealing at 150°C. The δ- phase $FAPbI_3$ immediately formed after depositing antisolvent (10 s), as indicated by the strong $(100)^{\delta}$ (q, the length of the reciprocal lattice vector, is 0.84 $Å^{-1}$), $(101)^{\delta}$, and $(110)^{\delta}$ diffraction planes (drawn in **Fig. S5**). Once the spin-coating is completed (30

s), the δ-phase persisted as 2D $BA_2FAPb_2I_7$ seeds began to crystallize at RT, illustrated by the out-of-plane $(400)^{2D}$ ($q = 0.65Å^{-1}$) and $(600)^{2D}$ ($q = 0.96Å^{-1}$) diffraction peaks (**Fig. S4**).

Next, a nonlinear stepwise annealing sequence was applied, in which the substrate temperature was increased by steps of 20°C in 20 second intervals up to 100°C and then increased by steps of 25°C up to 150°C (stage iii). Slow ramping to 150°C allowed us to observe the onset temperature of the $FAPbI_3$ α-phase. In this stage, for annealing at low temperatures (<100°C), the diffraction intensity of the 2D increased and a new peak emerged near $q = 1Å^{-1}$ corresponding to the $(001)^{3D}$ plane from α-phase $FAPbI_3$. **Fig. 2B, top** shows the integrated peak area for the $(100)^{\delta}$ and $(001)^{3D}$ peaks as a function of time for $FAPbI_3$ with 0.5 mol% BA n=2 incorporated. The $(001)^{3D}$ peak emerged after 75 s and slowly increases in intensity as the $(100)^{\delta}$ peak simultaneously decreases. Around after 130 s (T = 130°C), the remaining δ-phase abruptly converted into α-phase. As the film continued to anneal at 150°C for the remainder of the experiment (stage iv), the 2D diffraction peaks slowly faded and the α-phase $FAPbI_3$ peaks slowly grew more intense.

We repeated this experiment for four other types of precursor solutions. For additive-free $FAPbI_3$: **Fig. S6A** shows the in-situ contour WAXS plot for a 1:1 FAI:PbI_2 solution. In contrast to the $FAPbI_3$-2D sample, which exhibited a gradual emergence of α-phase between 100° and 150°C followed by a complete δ → α transformation at 130°C, the additive-free (control) $FAPbI_3$ showed a much more abrupt transition from δ-phase to α-phase near 150°C (**Fig. 2B, bottom**) consistent with previous reports. The $(001)^{3D}$ peak emerged later with a shorter tail in control $FAPbI_3$, and the $(100)^{\delta}$ peak did not prematurely decrease as in the film that incorporated BA n=2 We observed a much lower $(001)^{3D}$ peak intensity (relative to the $(100)^{\delta}$ peak intensity) for control pristine $FAPbI_3$ compared to $FAPbI_3$ with BA n=2 additive, suggesting a lowered crystallinity. Unlike the

film with added BA n=2, the $(001)^{3D}$ peak of control $FAPbI_3$ did not grow more intense as annealing at 150°C continued.

For a precursor solution of 1:1:35 mol% FAI: PbI_2: MACl in 4:1 DMF: DMSO, which is commonly used to grow phase stabilized $FAPbI_3$ *(25)*, the introduction of MA into the A-site of $FAPbI_3$ lowered the effective tolerance factor and stabilized the α-phase at a lower temperature compared to additive-free $FAPbI_3$. As a result, the abrupt $\delta \rightarrow \alpha$ transformation occurred at 75°C for the $FAPbI_3$-MACl sample (**Fig. S6B and S10A)**. However, like the control sample and in contrast to the 2D-templated sample, no region of gradual $\delta \rightarrow \alpha$ transformation was observed.

Next, BA n=2 was added to 1:1 PbI_2: FAI with concentrations of 0.25, 0.5, and 1.0 mol%. **Fig. S7** shows contour plots of the in-situ WAXS experiment for additive concentrations of 0.25 mol% (top) and 1.0 mol% (bottom). In all cases, the incorporation of BA n=2 increased the $(001)^{3D}$ peak intensity relative to the control, suggesting that even minute amounts of BA n=2 could improve α-phase crystallinity. The 0.5 mol% BA n=2 incorporated $FAPbI_3$ showed a similar film formation process to the 1.0 mol% sample discussed above, that is, a decrease in the $(100)^{\delta}$ peak and a slow emergence of the $(001)^{3D}$ peak at a lowered temperature. However, 0.25 mol% BA n=2 incorporation did not lower the onset temperature of the $(001)^{3D}$ peak relative to the control, and did not cause the same characteristic decrease in $(100)^{\delta}$ intensity below 150°C. The phase-stabilization appeared to be concentration invariant down to a certain minimum 2D concentration, below which the templating effect was lost but the film crystallinity was still improved.

We then examined a series of 2D additives including PA n=2, OA n=2, and PEA n=2. We note that the effect PA n=2 was similar to that of BA n=2, lowering the onset temperature of the α-phase peak and causing a decrease in the δ-phase below 150°C (**Fig. S8 and S10B**). In contrast, OA n=2 and PEA n=2 have markedly different effects (**Fig. S9 and S10B)**. For OA n=2, the 2D

peaks formed weakly and the α-phase emerged earlier than for the control sample, but no δ → α transformation was observed. Instead, the δ-phase persisted throughout annealing, suggesting that $OA_2FAPb_2I_7$ seeds could serve as nucleation sites for $FAPbI_3$ to a limited extent but slowed the δ → α transformation. $FAPbI_3$ with 0.5 mol% PEA n=2 additive showed no 2D peaks and no early α-phase emergence (**Fig. 2B, middle**). Moreover, $FAPbI_3$ with 1 mol% PEA n=2 also retained δ-phase peaks throughout the measurement, suggesting that the $PEA_2FAPb_2I_7$ not only failed to form seeds for templating $FAPbI_3$ but also suppressed δ → α transformation kinetics. **Fig. 2C** shows the azimuthally integrated WAXS patterns of $FAPbI_3$ samples with 1 mol% 2D, averaged across the first 90 s of annealing at 150°C. This plot revealed the incomplete δ → α transformation for the films incorporating 1 mol% OA and PEA n=2, contrasting with the complete transformation for 1 mol% BA and PA n=2 (also visible in **Fig. S10**). Interestingly, all 2D films showed a slow decrease in the 2D peak intensities and a slow increase in the $(001)^{3D}$ peak intensity during annealing at 150°C that was not observed for the control film (**Fig. 2B and Fig. S10**). Although gradual volatilization of the A' cation in $A'_2FAPb_2I_7$, leaving behind $FAPbI_3$ could account for these changes, as discussed below, optical and nuclear magnetic resonance (NMR) results suggest that the 2D phase was not completely lost to volatilization, and that there may be a competing mechanism of 2D restructuring within the lattice.

The in-situ WAXS results suggested that $BA_2FAPb_2I_7$ and $PA_2FAPb_2I_7$ could template α-phase $FAPbI_3$, but $OA_2FAPb_2I_7$ and $PEA_2FAPb_2I_7$ could not. Ex-situ 1D XRD was performed on separate 1 mol% 2D-incorporated $FAPbI_3$ films (**Fig. 2D**) and showed that $FAPbI_3$ films with added OA n=2 or PEA n=2 had an identical $(001)^{3D}$ interplanar spacing as control $FAPbI_3$, but that PA n=2 and BA n=2 caused a small but noticeable compression of the $(001)^{3D}$ interplanar spacing by -0.03% and -0.07%, respectively. Because the $(011)^{2D}$ interplanar spacing was lightly smaller

for BA n=2 than for PA n=2 (**Fig. 1A)**, a higher compressive strain for $FAPbI_3$ with added BA n=2 compared to PA n=2 also supports the (011) lattice templating hypothesis.

To verify our structural results, we performed similar in-situ optical spectroscopy measurements on the $BA_2FAPb_2I_7$-templated $FAPbI_3$ samples. During the initial stages of annealing, the film exhibited a strong excitonic absorption peak at 2.15 eV corresponding to $BA_2FAPb_2I_7$, which with progressive annealing transformed into α-$FAPbI_3$, characterized by a 3D perovskite absorption band edge (**Fig. S11**). Similarly, a strong emission of the $BA_2FAPb_2I_7$ perovskite was observed at 2.15 eV in the in-situ PL measurement, accompanied by a broad emission at lower energies (**Fig. S12**). We hypothesized that the lower energy emissions were from a combination of effects, including edge state emission *(45, 46)*, the formation of higher n-value 2D phases (e.g. n=3 $BA_2FA_2Pb_3I_{10}$) *(47,48)*, and quantum confinement effects of the 2D and $FAPbI_3$ crystallites *(49-52)*. Sub-bandgap edge state emission in $BA_2FAPb_2I_7$ was verified by spatially resolved PL, which showed a 1.8 eV PL emission peak only at the edges of an exfoliated $BA_2FAPb_2I_7$ single crystal. Additionally, the presence of a PL emission peak at 1.85eV and the observation of n=3 excitons in power-dependent PL indicate that FA intercalation increases the layer thickness from n=2 to n=3 during annealing. A similar broad emission below the n=2 bandgap was observed during film formation for $FAPbI_3$ with $PA_2FAPb_2I_7$ additive **(Fig. S12)**, consistent with the structural results for $PA_2FAPb_2I_7$ shown in **Fig. S8**. However, no sub-bandgap emission was observed for the control $FAPbI_3$ or for $FAPbI_3$ incorporating MACl, $OA_2FAPb_2I_7$, or $PEA_2FAPb_2I_7$ (**Fig. S13**).

Based on the in-situ WAXS and PL measurements in **Fig. 2** and **Fig. S2 to S10**, we propose the following film formation process mediated by 2D templating. The film first forms grains of *δ*-phase $FAPbI_3$ and 2D seeds at RT. The 2D likely formed initially because of its more negative

formation enthalpy, its RT phase-stability, and the presence of 2D seeds in the precursor solution as confirmed through dynamic light scattering (DLS) measurements shown in **Fig. S14**. During annealing, the δ-phase restructured itself beginning at the low-energy surfaces of the 2D seed crystals to form α-phase $FAPbI_3$. At the interface with $FAPbI_3$, the arrangement of PbI_6 octahedra in a 2D perovskite may facilitate nucleation of a stable α-phase $FAPbI_3$, with subsequent phase transformation toward the bulk *(53)*. Indeed, from **Fig. 2D**, we deduced that the growth mechanism favoured the formation of a compressively strained α-phase (001) plane templated by the 2D (011) interplanar spacing. The low-temperature α-phase formation being only observed for films with added PA and BA n=2, and these films being also the only ones to exhibit lattice strain, is strong evidence for a templating effect off the $(011)^{2D}$ spacing.

The (011) interplanar spacings of $BA_2FAPb_2I_7$ (6.359 Å) and $PA_2FAPb_2I_7$ (6.364 Å) are almost perfectly lattice matched with the $(001)^{3D}$ interplanar spacing of $FAPbI_3$, both falling within the range of reported $FAPbI_3$ lattice constants from 6.352 Å to 6.365 Å *(5,6)*, whereas the (011) interplanar spacings of $OA_2FAPb_2I_7$ (6.336 Å) and $PEA_2FAPb_2I_7$ (6.265 Å) were not well matched. This structural difference explains why OA-2D and PEA-2D did not show the same δ → α conversion process as BA-2D and PA-2D. The templating process and the resulting $FAPbI_3$ strain appeared 2D concentration-independent down to some minimum threshold, which for BA 2D perovskites was between 0.25 and 0.5 mol%. As the temperature was raised to 150°C and the sample continued to anneal, we hypothesize that the 2D perovskite simultaneously volatilized its A' cation and underwent a slow FA intercalation process, which increased its n-value.

Other reports have suggested that the A' cation of 2D perovskites incorporated into $FAPbI_3$ volatilized completely during annealing except for a small fraction left at grain boundaries,[19,37,38] which would also explain the disappearance of our 2D signal over time and the slow increase in

the $(001)^{3D}$ peak intensity during annealing at 150°C. Solid-state ^{1}H NMR on scraped films of $FAPbI_3$ with added 2D before and after annealing did reveal a partial volatilization of the spacer cation during film formation, but also confirmed appreciable fractions of BA and PA even after annealing at 150°C for 20 min (**Fig. S15** and **S16**). Time-of-flight secondary-ion mass spectrometry (ToF-SIMS) results suggested that the remaining 2D spacer cations were homogenously distributed up to 1 mol% and for higher concentrations, appeared more pronounced toward the film interface with the substrate (**Fig. S17**).

The BA and PA cations lead to the formation of a mixed 2D/3D phase that was challenging to characterize with the aforementioned long-range techniques. Instead, we applied high-field (21 T) solid-state NMR spectroscopy to resolve the local structures of the organic cations in the mixed phase (**Fig. S16**). The ^{1}H NMR peaks associated with the large (BA and PA) and small (FA) cations were well resolved so the amount of 2D phase present in the templated $FAPbI_3$ materials could be identified and quantified. In addition, the local structures of the mixed phases, elucidated by analysing 2D ^{1}H-^{1}H correlation NMR spectra (**Fig. S16, C to F**), showed the presence of through-space intermolecular interactions between the large cations (BA or PA) in the 2D phase and the small cations (FA) in the 3D $FAPbI_3$ phase. Based on the data presented above, we illustrate a comprehensive schematic diagram capturing the different stages of film formation in a 2D templated $FAPbI_3$ (**Fig. 2E and discussion in SI 1.18**).

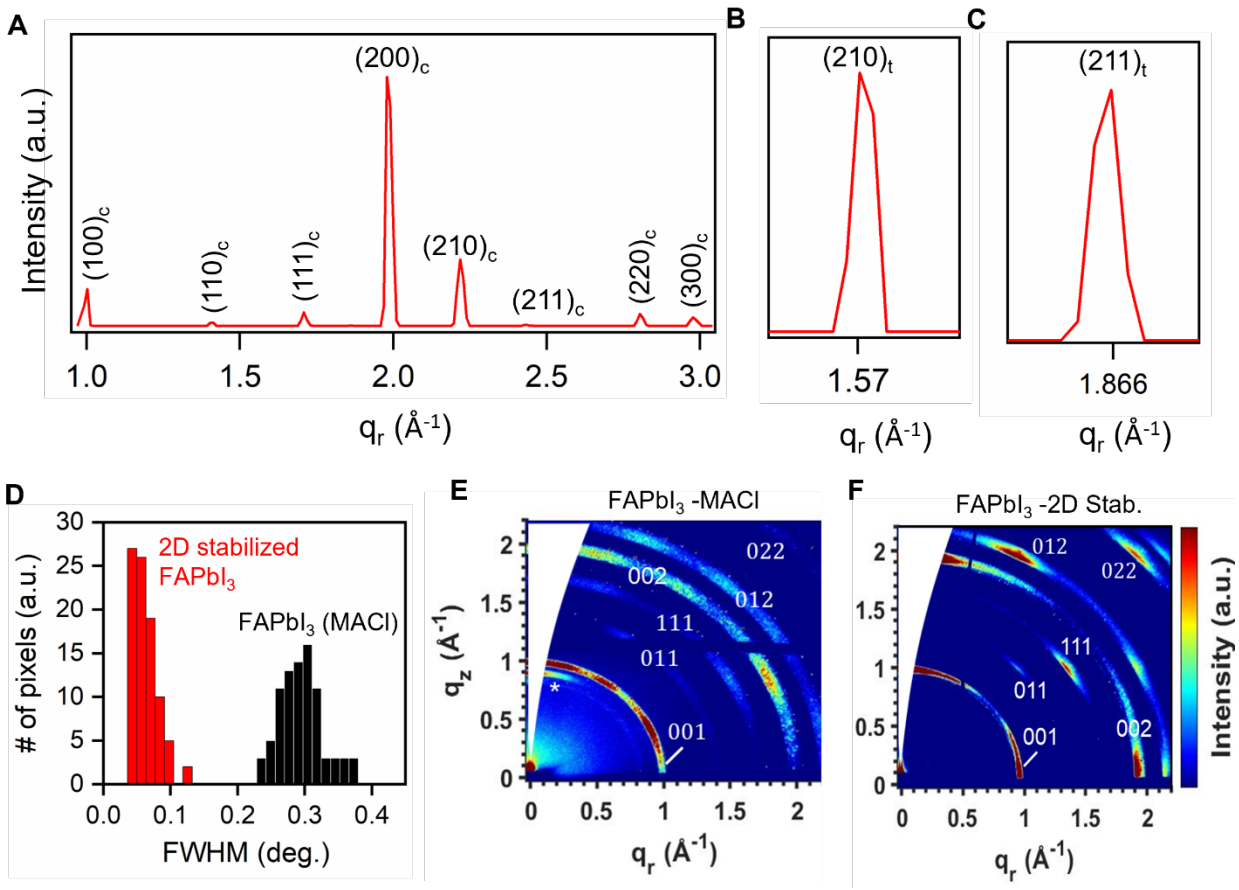

Fig. 3. Ex-situ structural characterization of phase stabilized $FAPbI_3$ films. A) A representative azimuthally integrated nano-XRD pattern for a film of $BA_2FAPb_2I_7$-templated $FAPbI_3$. **B**) The (210), and **C**) the (211) peaks of $BA_2FAPb_2I_7$-templated $FAPbI_3$ which can be seen after integrating several nano-XRD patterns obtained for different pixels within the testing region. These peaks are forbidden in a cubic crystal structure and confirm the existence of tetragonal $FAPbI_3$. **D**) A histogram of nano-XRD peak FWHM values for different pixels of a $BA_2FAPb_2I_7$-stabilized $FAPbI_3$ film (red) and a MACl-stabilized $FAPbI_3$ film (black). 2D-stabilized $FAPbI_3$ shows a significantly lower FWHM. **E** – **F**) Representative GIWAXS patterns for **E**) MACl-stabilized $FAPbI_3$ and **F**) $BA_2FAPb_2I_7$-stabilized $FAPbI_3$.

Structural and optical characteristics of Phase stabilized $FAPbI_3$

We hypothesized that the observed compressive lattice strain applied by the templating 2D phase can result in the formation of a locally segregated tetragonal structure *(54,55)*. To investigate the impact of 2D stabilization on nanoscale structural properties of $FAPbI_3$, we performed nanoscale XRD with a 25-nm spot size x-ray probe on MACl-stabilized $FAPbI_3$ and 2D-stabilized $FAPbI_3$. The high brilliance of a synchrotron light source enabled resolution of diffraction from minority

phases *(56,57)*. As shown in **Fig. S18**, both films showed sufficient x-ray stability to accommodate the measurement. Localized x-ray scattering from both cubic (i.e., α) and tetragonal phases was observed. A representative summed diffraction CCD image from a map of 2D-stabilized $FAPbI_3$ is shown in **Fig. S19**, and an azimuthally integrated pattern is shown in **Fig. 3A**. In addition to intense scattering from the cubic perovskite lattice, we observed two subtle peaks that we indexed to the tetragonal phase, the $(210)_t$ (t=tetragonal) at 1.57 A^{-1} and $(211)_t$ at 1.866 A^{-1} (**Fig. 3, B and C**). The $(211)_t$ peak could not be definitively indexed as tetragonal because of the overlapping $(210)_h$ (h=hexagonal, δ-phase) peak at virtually the same scattering vector, but the $(210)_t$ was unambiguously identified (*58*). Furthermore, because we observed no additional scattering peaks from the hexagonal phase in this sample, we also attribute the $(211)_t$ peak to the tetragonal phase. The diffraction from tetragonal phase was far less intense than diffraction from the cubic phase, with total summed diffraction intensity from the $(211)_t$ peak amounting to 0.8% of the intensity of the (200)c (c=cubic) peak (see **Fig. S19**).

To investigate the impacts of 2D stabilization on the quality of the perovskite crystallites in the thin film, we performed five-dimensional rocking curves (rocking curves with a two-dimensional detector and two-dimensional spatial mapping) on the sample where the angle of the incident x-ray was varied and spatial maps in the plane of the sample were repeated over the same area to precisely analyze the width of the diffraction peak. The 2D-stabilized $FAPbI_3$ exhibited substantially narrower diffraction full-width at half-maximum (FWHM) than the MACl-doped $FAPbI_3$ (**Fig. 3D**). The narrower diffraction peak could be a result of an increase in domain size or reduced microstructural disorder (microstrain) *(59)*. However, the well-established increase in domain size seen when MACl was included in perovskite precursors suggested that a smaller domain size in MACl-doped $FAPbI_3$ was not the cause *(25,60,61)*. We concluded that the 2D-

stabilization resulted in a reduced structural disorder within the crystallites of the thin film, which is consistent with previous reports *(53)*. Halder-Wagner analysis summarized in **Fig. S20** and **S21** further revealed that microstrain in 2D-stabilized $FAPbI_3$ decreased with increasing 2D concentration.

The grazing-incidence WAXS (GIWAXS) patterns of the MACl-doped $FAPbI_3$ perovskite thin films (**Fig. 3E**) and $FAPbI_3$ with $BA_2FAPb_2I_7$ additive revealed two different characteristics of the thin films. The MACl-doped $FAPbI_3$ films exhibited Bragg intensities extended along arc segments, indicating a random orientation of crystal domains or grains within a polycrystalline film (high mosaicity). Furthermore, these films showed PbI_2 diffraction peaks. In contrast, the 2D-stabilized $FAPbI_3$ films reveal well-defined Bragg diffraction spots along the (001) plane, observed along the Debye–Scherrer ring near $q = 1$ Å^{-1}. This distinct observation implied smaller mosaicity and improved grain orientation in the out-of-plane direction, perpendicular to the substrate. Furthermore, mosaicity appeared to be reduced with increasing 2D concentration (**Fig. S22)**. Atomic force microscopy (AFM) likewise showed an increase in $FAPbI_3$ grain size when 2D concentration was increased from 0.25 mol% to 0.5 mol%, although a further increase caused the grain size to decrease (**Fig. S23)**. These results were consistent with the observation in **Fig. S7** of improved crystallinity for $FAPbI_3$ films incorporating even small amounts of BA n=2.

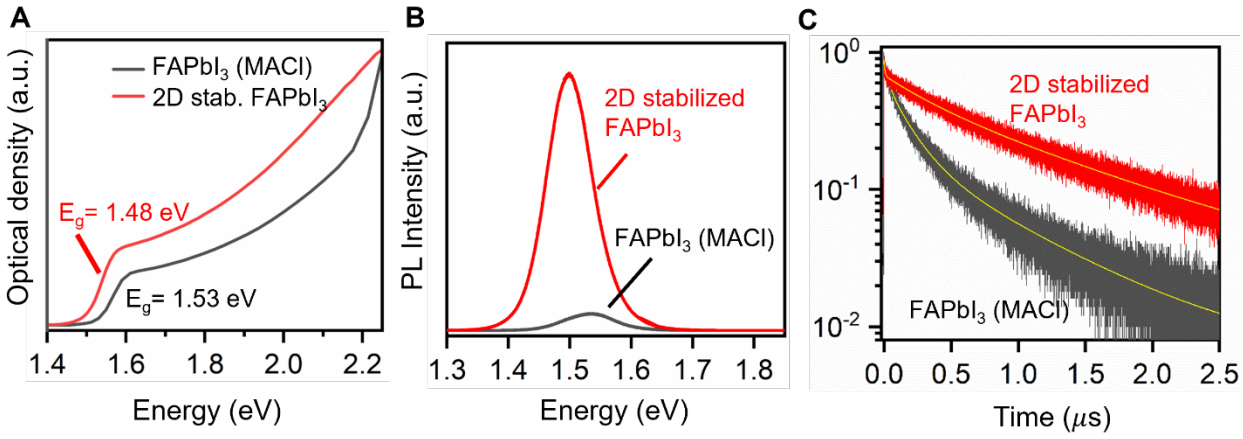

Fig. 4. Optical characterization of the phase stabilized $FAPbI_3$ films. A) Absorption spectra of MACl-stabilized $FAPbI_3$ (grey) and $BA_2FAPb_2I_7$-stabilized $FAPbI_3$ (red) with their band gaps indicated. **B**) PL spectra of MACl-stabilized $FAPbI_3$ (gray) and $BA_2FAPb_2I_7$-stabilized $FAPbI_3$ (red). **C**) TRPL spectra of MACl-stabilized $FAPbI_3$ (gray) and $BA_2FAPb_2I_7$-stabilized $FAPbI_3$ (red).

We observed an increase in the absorption of the 2D stabilized $FAPbI_3$ compared to the MACl-doped $FAPbI_3$. (**Fig. 4A**). Using the Tauc plot calculated from the absorption spectrum (**Fig. S24**), we derived a bandgap of 1.48 eV for the 2D stabilized $FAPbI_3$ (versus the 1.52 eV band gap of the MACl-doped films) that was much closer to the smallest reported (1.45 eV) bandgap of $FAPbI_3$ *(5)*. This band gap reduction (**Fig. 4A-B**) was consistent with experimental signatures pointing toward a reduction of the lattice disorder (**Fig. 3E-F**) *(53)*. In a polymorphous picture of the cubic phase of $FAPbI_3$, the reduction of polymorphism also leads to reduced tilt amplitudes *(4,62)*. As 2D concentration increased, the valence band maximum (VBM) was lowered (**Fig. S25)** and the band gap widened.

We also observed an order of magnitude increase in the PL intensity of the 2D-stabilized $FAPbI_3$ compared to the MACl-doped $FAPbI_3$ indicating reduced nonradiative recombination (**Fig. 4B**). The PL peak positions aligned with the absorption thresholds for both the films. In time-resolved PL measurements (**Fig. 4C**), the 2D stabilized $FAPbI_3$ film exhibited a slower PL decay rate compared to the reference, implying a decrease in nonradiative recombination attributable to a reduction in trap-mediated bulk or surface recombination processes.

Photovoltaic studies

We used 2D stabilized $FAPbI_3$ to fabricate perovskite solar cells using an inverted architecture with MeO-2PACz as the hole transport layer and C_{60} as the electron transport layer. To construct a band diagram of the device architecture (**Fig. 5A**), we measured the valence band maxima and conduction band minima of the MACl-doped $FAPbI_3$ and 2D stabilized $FAPbI_3$ by combining photoemission yield spectroscopy (PES) and absorption measurements. The details of the

measurements are discussed in the methods section of the SI. The 2D stabilized $FAPbI_3$ although slightly shifted toward higher energy compared to the MACl-doped $FAPbI_3$ had an appropriate band alignment for charge carrier separation and extraction.

The current density-voltage (*J–V*) characteristics of the best-performing 2D stabilized $FAPbI_3$ device in reverse and forward bias sweeps are illustrated in **Fig. 5B**. We achieved a power conversion efficiency (PCE) of 24.1% for an active area of 0.5 cm^2 under AM1.5G illumination (**Fig. 5E**) with a short circuit current density (J_{SC}) of 25.5 $mA.cm^{-2}$, open circuit voltage (V_{OC}) of 1.12 V, and fill factor of 82%. These metrics compare favourably with the corresponding thermodynamic limits of 31.1 $mA{\cdot}cm^{-2}$, 1.21 V, and 89%, respectively *(63)*. **Fig. 5C** shows the external quantum efficiency (EQE) for the same device as that of the *J–V* curve. Solar cells under identical conditions using different 2D perovskite concentration were fabricated to confirm the impact of concentration on performance. The statistical distributions of J_{SC}, V_{OC}, fill factor (FF), and PCE for 40 devices of each condition are shown in **Fig. S26**. The J_{SC} obtained by integrating the EQE over the wavelength is 24.3 $mA\ cm^{-2}$, which was in good agreement with that of the device's *J–V* curve measured using a solar simulator. For comparison, we fabricated $FAPbI_3$ devices stabilized using $PA_2FAPb_2I_7$, $OA_2FAPb_2I_7$ and $PEA_2FAPb_2I_7$ (see **Fig. S27)**. The PA-templated $FAPbI_3$ device exhibited a PCE of 21%, with a Jsc of 25.2 mA.cm-2, V_{OC} of 1.06V, and FF of 78.1%. In the case of optimized OA- and PEA-templated $FAPbI_3$, we achieved PCEs of 16.54% (J_{sc} of 23.93 mA.cm-2, V_{OC} of 0.97V, and FF of 71%) and 14.65% (Jsc of 23.15 $mA.cm^{-2}$, V_{OC} of 0.96V, and FF of 65%), respectively.

Finally, we compared the intrinsic and operational stability of undoped, $BA_2FAPb_2I_7$-templated, and MACl-doped $FAPbI_3$ films and devices. The 2D-templated $FAPbI_3$ was exceptionally stable under a variety of conditions compared to both undoped and MACl-doped

$FAPbI_3$. The shelf stability of 2D-stabilized $FAPbI_3$ films showed a significant improvement compared to undoped $FAPbI_3$ (**Fig. S28**). We also performed in-situ GIWAXS measurements (**Fig. S29)** to compare the stability of MACl-doped and $BA_2FAPb_2I_7$-incorporated $FAPbI_3$ devices in a >90%RH environment at 65ºC with 1-Sun illumination. The 2D-templated $FAPbI_3$ device showed minimal $\alpha \rightarrow \delta$ conversion over 170 min in the degrading environment. In contrast, the δ-phase became dominant in the MACl-doped $FAPbI_3$ device within the first 15 min of measurement. The much higher stability of the 2D-templated $FAPbI_3$ device in this experiment corroborated the maximum power point tracking (MPPT) device stability tests shown in **Fig. 5D** for 2D-templated $FAPbI_3$ and MACl-doped $FAPbI_3$.

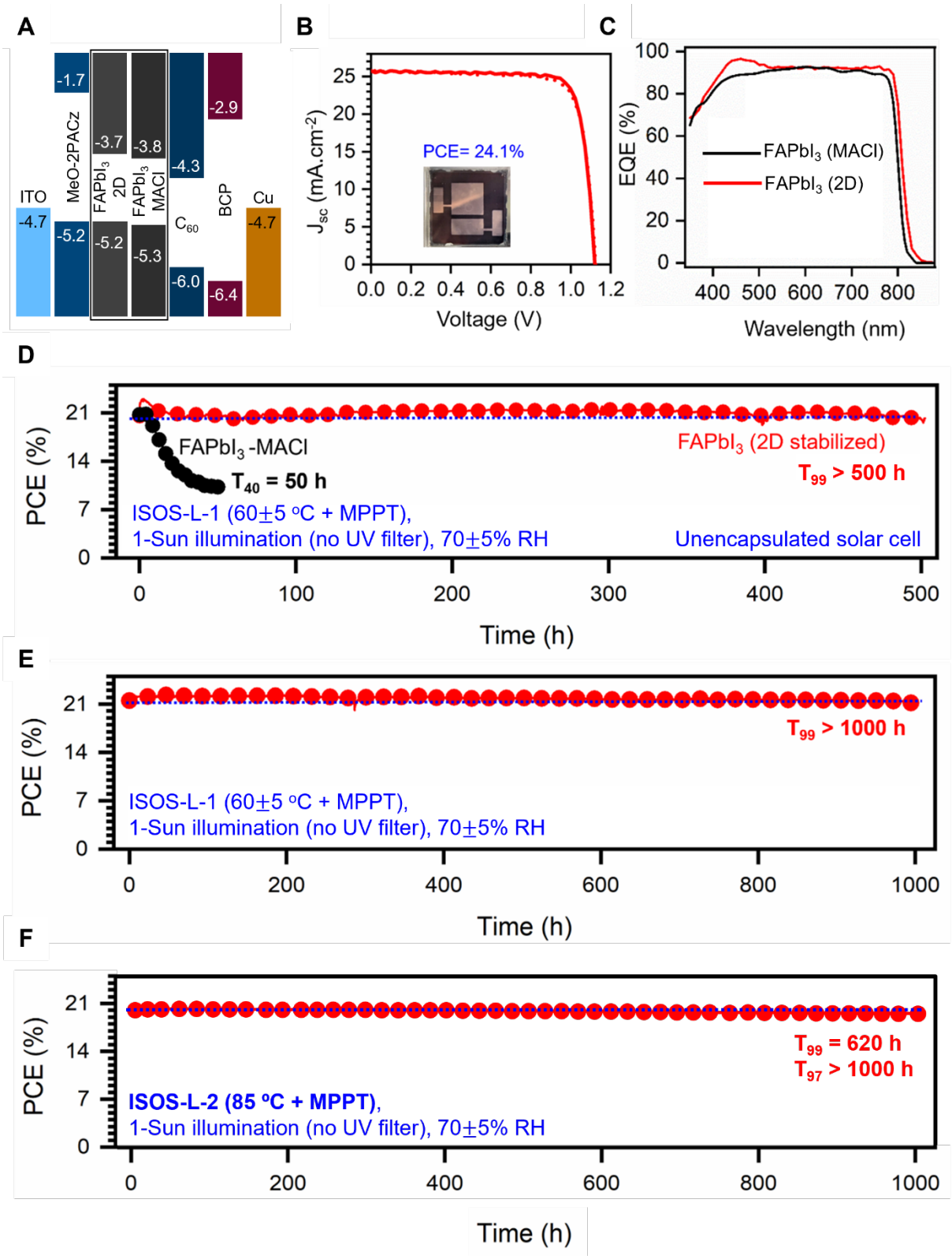

Figure 5: 2D-stabilized $FAPbI_3$ device performance. A) Device architecture of best-performing device showing band alignment of each layer. **B**) The J-V curve of the champion device shows

both a forward sweep (solid line) and reverse sweep (dashed line). The inset shows a real image of the device. **C**) The EQE of the champion 2D-stabilized $FAPbI_3$ device compared to the champion MACl-stabilized $FAPbI_3$ device. **D-F**) Stability tests on 2D stabilized $FAPbI_3$. **D**) Unencapsulated 2D-$FAPbI_3$ (red) and MACl-$FAPbI_3$ (black) cell under 1-sun illumination at 60°C with MPP tracking, in ambient air. **E**) Encapsulated cell under 1-sun illumination at 60°C with MPP tracking. **F**) Encapsulated cell under 1-sun illumination at 85°C with MPP tracking.

We evaluated the device stability with standard interfaces. We first performed measurements on unencapsulated p-i-n solar cells in ambient air under 1-Sun illumination (no UV filter) with MPPT. As shown in **Fig. 5D**, the 2D-templated devices showed almost no PCE drop during the first 500 hours of operation with T_{99}>500 h. In contrast, the unencapsulated MACl-doped $FAPbI_3$ sample degraded within the first 50 hr of operation showing a T_{40}=50 h. Further, as shown in **Fig. 5E**, an encapsulated 2D-templated $FAPbI_3$ device showed almost no efficiency drop from an initial 21% PCE for more than 1000 hours (T_{99}>1000 hr) of continuous 1-Sun illumination at MPPT in ambient air (ISOS-L-1 protocol). This stability is among the best reported for $FAPbI_3$-based perovskite devices, which in recent reports *(26,27,36)* have been measured under inert conditions.

The encapsulated solar cells were additionally measured under 1-sun illumination at MPPT at 85°C on a hot plate in the ambient atmosphere (ISOS-L-2 protocol), as shown in **Fig. 5F**. The 2D-stabilized $FAPbI_3$ devices retained 99% of their initial PCE after 620 hours, and more than 97% of their initial PCE after 1000 hours. Using the rule of thumb from Si photovoltaics that a 10°C increase in temperature translates to a 2x increase in degradation rate *(64)*, a T_{97} = 1000 hours at 85°C corresponds to a T_{97} = 16000 hours (1.8 years) at 45°C. This result is a critical step towards a $FAPbI_3$-based device with commercially-relevant stability.

Discussion

In summary, our investigation unveils a unique approach to achieve a highly stable black phase of $FAPbI_3$, even at temperatures considerably lower than the δ-$FAPbI_3$ to α-$FAPbI_3$ transition temperature. This method involves templating the (001) interplanar spacing of 3D $FAPbI_3$ to the (011) interplanar spacing of carefully selected 2D perovskites with FA as the cage cation, considering the respective Pb-Pb interatomic spacing for each structure. Detailed characterization, incorporating correlated WAXS, optical absorbance, and PL, indicates that the resulting black $FAPbI_3$ phase exhibits a lattice constant corresponding to the $d_{(011)}$ interplanar spacing of the underlying 2D perovskite. We extend this templating strategy to scalable solution-processed methods by introducing pre-synthesized 2D perovskite seeds to $FAPbI_3$ precursor solutions. During the film formation, the phase-stable 2D perovskite nucleates first due to its lower enthalpy of formation and stability at room temperature. The 2D structure acts as a seed on which the 3D perovskite to adopt the underlying 2D lattice periodicity, allowing for the preferential templating of the 3D perovskite on the 2D phase during subsequent film annealing. The resulting bulk $FAPbI_3$ films exhibit an energy gap (E_g) of 1.48 eV and demonstrate exceptional durability under aggressive conditions, achieving a remarkable PCE of 24.1% in a p-i-n device architecture on a 0.5 cm^2 device area. These outcomes validate a novel design strategy for the templated growth of 3D perovskites using 2D perovskites and will enable new physical behaviours and properties and functionalities relevant for optoelectronic devices. We anticipate that such strategies might extend beyond perovskites, potentially using other molecular and organic systems with comparable lattice constants to produce epitaxial kinetically stabilized materials.

REFERENCES

1. Masi, S., Gualdrón-Reyes, A. F. & Mora-Seró, I. Stabilization of Black Perovskite Phase in FAPbI3 and CsPbI3. *ACS Energy Lett.* **5**, 1974–1985 (2020).
2. Huang, Y. *et al.* The intrinsic properties of FA(1−x)MAxPbI3 perovskite single crystals. *J. Mater. Chem. A* **5**, 8537–8544 (2017).
3. Tao, S. *et al.* Absolute energy level positions in tin-and lead-based halide perovskites. *Nature communications* **10**, 2560 (2019).
4. Zhao, X.-G., Dalpian, G. M., Wang, Z. & Zunger, A. Polymorphous nature of cubic halide perovskites. *Phys. Rev. B* **101**, 155137 (2020).
5. Stoumpos, C. C., Malliakas, C. D. & Kanatzidis, M. G. Semiconducting Tin and Lead Iodide Perovskites with Organic Cations: Phase Transitions, High Mobilities, and Near-Infrared Photoluminescent Properties. *Inorg. Chem.* **52**, 9019–9038 (2013).
6. Kawachi, S. *et al.* Structural and Thermal Properties in Formamidinium and Cs-Mixed Lead Halides. *J. Phys. Chem. Lett.* **10**, 6967–6972 (2019).
7. Kieslich, G., Sun, S. & Cheetham, A. K. An extended tolerance factor approach for organic–inorganic perovskites. *Chemical science* **6**, 3430–3433 (2015).
8. Ferreira, A. C. *et al.* Elastic softness of hybrid lead halide perovskites. *Physical Review Letters* **121**, 085502 (2018).
9. Li, Z. *et al.* Stabilizing perovskite structures by tuning tolerance factor: formation of formamidinium and cesium lead iodide solid-state alloys. *Chemistry of Materials* **28**, 284–292 (2016).
10. Saliba, M. *et al.* Cesium-containing triple cation perovskite solar cells: improved stability, reproducibility and high efficiency. *Energy & environmental science* **9**, 1989–1997 (2016).
11. Jeon, N. J. *et al.* Compositional engineering of perovskite materials for high-performance solar cells. *Nature* **517**, 476–480 (2015).

12. Entropy-driven structural transition and kinetic trapping in formamidinium lead iodide perovskite | Science Advances. https://www.science.org/doi/10.1126/sciadv.1601650.
13. Green, M. A. *et al.* Solar cell efficiency tables (version 62). *Progress in Photovoltaics: Research and Applications* **31**, 651–663 (2023).
14. Min, H. *et al.* Perovskite solar cells with atomically coherent interlayers on SnO2 electrodes. *Nature* **598**, 444–450 (2021).
15. Yoo, J. J. *et al.* Efficient perovskite solar cells via improved carrier management. *Nature* **590**, 587–593 (2021).
16. Jeong, J. *et al.* Pseudo-halide anion engineering for α-FAPbI3 perovskite solar cells. *Nature* **592**, 381–385 (2021).
17. Kim, M. *et al.* Conformal quantum dot–SnO2 layers as electron transporters for efficient perovskite solar cells. *Science* **375**, 302–306 (2022).
18. Jeong, M. J. *et al.* Boosting radiation of stacked halide layer for perovskite solar cells with efficiency over 25%. *Joule* **7**, 112–127 (2023).
19. Park, J. *et al.* Controlled growth of perovskite layers with volatile alkylammonium chlorides. *Nature* 1–3 (2023) doi:10.1038/s41586-023-05825-y.
20. Zhao, Y. *et al.* Inactive (PbI2)2RbCl stabilizes perovskite films for efficient solar cells. *Science* **377**, 531–534 (2022).
21. Jiang, Q. *et al.* Surface reaction for efficient and stable inverted perovskite solar cells. *Nature* **611**, 278–283 (2022).
22. Li, Z. *et al.* Organometallic-functionalized interfaces for highly efficient inverted perovskite solar cells. *Science* **376**, 416–420 (2022).
23. Zhu, Z. *et al.* Correlating the perovskite/polymer multi-mode reactions with deep-level traps in perovskite solar cells. *Joule* **6**, 2849–2868 (2022).
24. Li, G. *et al.* Highly efficient p-i-n perovskite solar cells that endure temperature variations. *Science* **379**, 399–403 (2023).

25. Kim, M. *et al.* Methylammonium Chloride Induces Intermediate Phase Stabilization for Efficient Perovskite Solar Cells. *Joule* **3**, 2179–2192 (2019).

26. Min, H. *et al.* Efficient, stable solar cells by using inherent bandgap of α-phase formamidinium lead iodide. *Science* **366**, 749–753 (2019).

27. Park, B. *et al.* Stabilization of formamidinium lead triiodide α-phase with isopropylammonium chloride for perovskite solar cells. *Nat Energy* **6**, 419–428 (2021).

28. Hui, W. *et al.* Stabilizing black-phase formamidinium perovskite formation at room temperature and high humidity. *Science* **371**, 1359–1364 (2021).

29. Lee, J.-W., Seol, D.-J., Cho, A.-N. & Park, N.-G. High-Efficiency Perovskite Solar Cells Based on the Black Polymorph of HC(NH2)2PbI3. *Advanced Materials* **26**, 4991–4998 (2014).

30. Kim, G. *et al.* Impact of strain relaxation on performance of α-formamidinium lead iodide perovskite solar cells. *Science* **370**, 108–112 (2020).

31. Park, Y. H. *et al.* Inorganic Rubidium Cation as an Enhancer for Photovoltaic Performance and Moisture Stability of HC(NH2)2PbI3 Perovskite Solar Cells. *Advanced Functional Materials* **27**, 1605988 (2017).

32. Alanazi, A. Q. *et al.* Benzylammonium-Mediated Formamidinium Lead Iodide Perovskite Phase Stabilization for Photovoltaics. *Advanced Functional Materials* **31**, 2101163 (2021).

33. Alanazi, A. Q. *et al.* Atomic-Level Microstructure of Efficient Formamidinium-Based Perovskite Solar Cells Stabilized by 5-Ammonium Valeric Acid Iodide Revealed by Multinuclear and Two-Dimensional Solid-State NMR. *J. Am. Chem. Soc.* **141**, 17659–17669 (2019).

34. Hu, R. *et al.* Enhanced stability of α-phase FAPbI 3 perovskite solar cells by insertion of 2D (PEA) 2 PbI 4 nanosheets. *Journal of Materials Chemistry A* **8**, 8058–8064 (2020).

35. Huang, Y. *et al.* Low-Temperature Phase-Transition for Compositional-Pure α-FAPbI3 Solar Cells with Low Residual-Stress and High Crystal-Orientation. *Small Methods* **6**, 2200933 (2022).

36. Lee, J.-W. *et al.* 2D perovskite stabilized phase-pure formamidinium perovskite solar cells. *Nat Commun* **9**, 3021 (2018).

37. Liang, J. *et al.* Volatile 2-Thiophenemethylammonium and Its Strongly Bonded Condensation Product for Stabilizing α-FAPbI3 in Sequential-Deposited Solar Cells. *ACS Materials Lett.* **5**, 1395–1400 (2023).

38. Liang, J. *et al.* Volatile 2D Ruddlesden-Popper Perovskite: A Gift for α-Formamidinium Lead Triiodide Solar Cells. *Advanced Functional Materials* 2207177 (2022).

39. Shen, C. *et al.* Stabilizing Formamidinium Lead Iodide Perovskite by Sulfonyl-Functionalized Phenethylammonium Salt via Crystallization Control and Surface Passivation. *Solar RRL* **4**, 2000069 (2020).

40. Shi, P. *et al.* Oriented nucleation in formamidinium perovskite for photovoltaics. *Nature* 1–5 (2023) doi:10.1038/s41586-023-06208-z.

41. Sidhik, S. *et al.* Memory Seeds Enable High Structural Phase Purity in 2D Perovskite Films for High-Efficiency Devices. *Adv. Mater.* **33**, 2007176 (2021).

42. Sidhik, S. *et al.* High-phase purity two-dimensional perovskites with 17.3% efficiency enabled by interface engineering of hole transport layer. *Cell Reports Physical Science* **2**, 100601 (2021).

43. Metcalf, I. *et al.* Synergy of 3D and 2D Perovskites for Durable, Efficient Solar Cells and Beyond. *Chem. Rev.* **123**, 9565–9652 (2023).

44. Hou, J., Li, W., Zhang, H., Sidhik, S., Fletcher, J., Metcalf, I., Anantharaman, S.B., Shuai, X., Mishra, A., Blancon, J.C. and Katan, C. Synthesis of 2D perovskite crystals via progressive transformation of quantum well thickness. *Nature Synthesis*, **pp.1-11,** (2023).

45. Blancon, J.-C., Even, J., Stoumpos, Costas. C., Kanatzidis, Mercouri. G. & Mohite, A. D. Semiconductor physics of organic–inorganic 2D halide perovskites. *Nat. Nanotechnol.* **15**, 969–985 (2020).

46. Blancon, J.-C. *et al.* Extremely efficient internal exciton dissociation through edge states in layered 2D perovskites. *Science* **355**, 1288–1292 (2017).

47. Blancon, J.-C. *et al.* Scaling law for excitons in 2D perovskite quantum wells. *Nat Commun* **9**, 2254 (2018).

48. Stoumpos, C. C. *et al.* Ruddlesden–Popper Hybrid Lead Iodide Perovskite 2D Homologous Semiconductors. *Chem. Mater.* **28**, 2852–2867 (2016).

49. Even, J., Pedesseau, L. & Katan, C. Understanding quantum confinement of charge carriers in layered 2D hybrid perovskites. *ChemPhysChem* **15**, 3733–3741 (2014).

50. Tamarat, P. *et al.* Universal scaling laws for charge-carrier interactions with quantum confinement in lead-halide perovskites. *Nature Communications* **14**, 229 (2023).

51. Sapori, D., Kepenekian, M., Pedesseau, L., Katan, C. & Even, J. Quantum confinement and dielectric profiles of colloidal nanoplatelets of halide inorganic and hybrid organic–inorganic perovskites. *Nanoscale* **8**, 6369–6378 (2016).

52. Katan, C., Mercier, N. & Even, J. Quantum and dielectric confinement effects in lower-dimensional hybrid perovskite semiconductors. *Chemical reviews* **119**, 3140–3192 (2019).

53. Song, S. *et al.* Molecular Engineering of Organic Spacer Cations for Efficient and Stable Formamidinium Perovskite Solar Cell. *Advanced Energy Materials* **10**, 2001759 (2020).

54. Doherty, T. A. S. *et al.* Stabilized tilted-octahedra halide perovskites inhibit local formation of performance-limiting phases. *Science* **374**, 1598–1605 (2021).

55. Beal, R. E. *et al.* Structural Origins of Light-Induced Phase Segregation in Organic-Inorganic Halide Perovskite Photovoltaic Materials. *Matter* **2**, 207–219 (2020).

56. Winarski, R. P. *et al.* A hard X-ray nanoprobe beamline for nanoscale microscopy. *J Synchrotron Rad* **19**, 1056–1060 (2012).

57. Li, N. *et al.* Microscopic degradation in formamidinium-cesium lead iodide perovskite solar cells under operational stressors. *Joule* **4**, 1743–1758 (2020).

58. Weber, O. J. *et al.* Phase Behavior and Polymorphism of Formamidinium Lead Iodide. *Chem. Mater.* **30**, 3768–3778 (2018).

59. Ungár, T. Microstructural parameters from X-ray diffraction peak broadening. *Scripta Materialia* **51**, 777–781 (2004).

60. Li, Y. *et al.* CH3NH3Cl Assisted Solvent Engineering for Highly Crystallized and Large Grain Size Mixed-Composition (FAPbI3)0.85(MAPbBr3)0.15 Perovskites. *Crystals* **7**, 272 (2017).

61. Ye, F. *et al.* Roles of MACl in Sequentially Deposited Bromine-Free Perovskite Absorbers for Efficient Solar Cells. *Advanced Materials* **33**, 2007126 (2021).

62. Zacharias, M., Volonakis, G., Giustino, F. & Even, J. Anharmonic electron-phonon coupling in ultrasoft and locally disordered perovskites. *npj Comput Mater* **9**, 1–13 (2023).

63. Alam, M. A. & Khan, M. R. *Principles of solar cells: connecting perspectives on device, system, reliability, and data science*. (World Scientific Publishing Co. Pte. Ltd, 2022).

64. Boyd, C. C., Cheacharoen, R., Leijtens, T. & McGehee, M. D. Understanding Degradation Mechanisms and Improving Stability of Perovskite Photovoltaics. *Chem. Rev.* **119**, 3418–3451 (2019).

Acknowledgements

In situ diffraction experiments were conducted at the Advanced Light Source (ALS) beamline 12.3.2 supported by Nobumichi Tamura, which is a US Department of Energy Office (DOE) of Science user facility under contract DE-AC02-05CH11231. The authors thank J. Slack from the ALS for development and maintenance of the in situ spin coater. GIWAXS experiments utilized the X-ray scattering partner user program at the Center for Functional Nanomaterials (CFN) and used beamline 11-BM (CMS) of the National Synchrotron Light Source II. Both facilities are US Department of Energy (DOE) Office of Science user facilities operated for the DOE Office of Science by Brookhaven National Laboratory under contract no. DE-SC0012704. The authors are grateful to R. Li for assistance with GIWAXS. Nanodiffraction experiments made use of the Center for Nanoscale Materials and Advanced Photon Source, both Office of Science user facilities, which were supported by the US DOE, Office of Science, Office of Basic Energy Sciences, under contract no. DE-AC02-06CH11357. The authors are grateful to M. Holt and T. Zhou for their guidance and assistance with nanodiffraction. The authors are grateful to T. Terlier for the measurement and analysis of ToF-SIMS data.

Funding:
The work at Rice University was supported by the DOE- EERE DE-EE0010738 program. I.M. acknowledges financial support from the Hertz Foundation and the National Science Foundation Graduate Research Fellowship Program. This material is based on work supported by the National Science Foundation Graduate Research Fellowship Program under grant NSF 20-587. This research used resources of the Advanced Photon Source, a US DOE Office of Science user facility operated for the DOE Office of Science by Argonne National Laboratory under contract DE-AC02- 06CH11357. The work at ISCR and Institut FOTON was performed with funding from the European Union's Horizon 2020 research and innovation program (EU-H2020) under grant 861985 (PeroCUBE). A.B. was supported by a fellowship through the National Defense Science and Engineering Graduate Fellowship Program (NDSEG) sponsored by the Air Force Research

Laboratory (AFRL), the Office of Naval Research (ONR), and the Army Research Office (ARO). J.H. acknowledges financial support from the China Scholarship Council (grant 202107990007). D.G. acknowledges ONR N00014-20-1-2587 for supporting his effort. J.E. acknowledges financial support from the Institut Universitaire de France. Work at the Molecular Foundry was supported by the Office of Science, Office of Basic Energy Sciences, of the US DOE under contract DE-AC02-05CH11231. T.K. acknowledges funding by the German Science Foundation (DFG, fellowship no. KO6414). D.P.F. acknowledges financial support for the synchrotron-based x-ray characterization from the National Science Foundation (DMR 1848371). G.N.M.R. acknowledges financial support from EU- H2020 grant 795091 and IR INFRANALYTICS FR2040 for carrying out NMR experiments.

Authors contributions:
A.D.M. and J.E. conceived of the idea, designed the experiments, analyzed the data, and co-wrote the manuscript. S.S., W.L., and I.M. designed the experiments, analyzed the data, and co-wrote the manuscript. S.S. fabricated and tested devices and performed templating experiments, WAXS measurements, in situ PL measurements, and stability experiments. I.M. fabricated and tested devices, synthesized 2D crystals, and performed WAXS measurements, GIWAXS measurements, and in situ PL measurements. W.L. and E.T. performed and analyzed the GIWAXS measurements. T.K. performed WAXS measurements and performed in situ PL measurements under the guidance of C.M.S.-F. C.J.D. and A.T. performed nano-XRD measurements and analyzed the data under the guidance of D.P.F. M.K. performed the DLS of FAPbI3 solutions under the guidance from A.M. J.H. synthesized the 2D perovskite crystals. F.M., J.P., and R.G. fabricated devices, tested devices, and helped in performing the stability experiments. H.Z. performed ex situ optical measurements with the help from A.T. I.A.M.P. performed and analyzed the solid-state NMR measurements under the guidance of G.N.M.R. A.B. performed the PES measurements for the perovskite thin films under the guidance of M.G.K. M.A.A. analyzed device performance. C.K. analyzed the structural properties of 2D and lattice mismatch between the 2D and 3D perovskites. D.G. analyzed the optical spectroscopy measurements and contributed to editing the paper.

Competing interests: Rice University has filed a patent for a method of fabricating the 2D-templated phase-pure $FAPbI_3$ perovskite.

Data and Materials Availability: All data needed to evaluate the conclusions in the paper are present in the paper or the Supplementary Materials.